Controlled Shell and Kernel Modifications of Atomically Precise Pd/Ag Superatomic Nanoclusters

Yu-Rong Ni, Michael N Pillay, Tzu-Hao Chiu, Ying-Yann Wu, Samia Kahlal, Jean-Yves Saillard, Chen-Wei Liu

Controlled Shell and Kernel Modifications of Atomically Precise Pd/Ag Superatomic Nanoclusters

Yu-Rong Ni,[a] Michael N. Pillay,[a] Tzu-Hao Chiu,[a] Ying-Yann Wu,[a] Samia Kahlal,[b] and Jean-Yves Saillard,*[b] and C. W. Liu*[a]

Dedication ((optional))

[a] Y. -R. Ni, Dr. M. N. Pillay, T. –H. Chiu, Dr. Y. -Y. Wu, Prof. Dr. C. W. Liu
Department of Chemistry
National Dong Hwa University
No. 1, Sec 2, Da Hsueh Rd., Hualien 97401 (Taiwan, R.O.C.)
E-mail: chenwei@gms.ndhu.edu.tw
[b] Dr. S. Kahlal, Prof. Dr. J. -Y. Saillard
CNRS, ISCR-UMR 6226
Univ Rennes
F-35000 Rennes, France
E-mail: jeanyves.saillard@univ-rennes1.fr

Supporting information for this article is given via a link at the end of the document.

Abstract: The first 8-electron Pd/Ag superatomic alloys with an interstitial hydride $[PdHAg_{19}(dtp)_{12}]$ (dtp = $S_2P(O^iPr)_2^-$) **1** and $[PdHAg_{20}(dtp)_{12}]^+$ **2** are reported. The targeted addition of a single Ag atom to **1** is achieved by the reaction of one equivalent of trifluoroacetic acid, resulting in the formation of **2** in 55 % yield. Further modification of the shell results in the formation of $[PdAg_{21}(dtp)_{12}]^+$ **3** via an internal redox reaction, with the system retaining an 8-electron superatomic configuration. The interstitial hydride in **1** and **2**, contributes its $1s^1$ electron to the superatomic electron count, and occupies a $PdAg_3$ tetrahedron. The distributions of isomers corresponding to different dispositions of the outer capping Ag atoms are investigated by multinuclear VT-NMR spectroscopy. The emissive state of **3** has a lifetime of 200 µs (λex =448; λem =842), while **1** and **2** are non-emissive. The catalytic reduction of 4-nitrophenol is demonstrated with **1**-**3** at room temperature.

Introduction

Palladium hydride chemistry has a rich history, dating back to 1869 when T. Graham was perhaps the first one to identify the hydrogen-palladium combination as an alloy and the ability of palladium to restrain the volatility of hydrogen.[1] The hydride atom plays a crucial role in the era of atomic precise nanoclusters (NC) and in particular superatomic cluster formation. The evolution in the understanding of the superatomic concept began with exploiting the stability of NC electronic closed shells, yielding a new class of compounds with unique properties, different from that of bulk metal.[2] In this field, the chemistry of superatomic gold NCs has been particularly prolific in providing valuable data on the superatomic concept, both from theoretical and experimental approaches.[3,4] Structural determination by X-ray crystallography and charge determination by mass spectrometry provide crucial evidence for the identification of superatomic species.[5] Ligand-protected silver superatomic constructs are often based on a centered icosahedral kernel encapsulated in larger structures.[6,7] The contribution of the Pd atom to the superatomic electron count in silver-doped species has been demonstrated to be zero.[8–11]

The role of hydrides in superatomic kernels in forming silver superatomic NCs is dual in nature. They provide the necessary reduction of metal centers in the formation of superatomic frameworks, as well as an H atom which contributes its valuable $1s^1$ electron to the kernel in both *homo*- and *hetero*-metallic systems.[12–19] Although discrete palladium hydride motifs have been established in traditional coordination chemistry, few examples of a PdH unit encapsulated within a metallic framework have been realized.[20] NCs encaging the PdH motif are a relatively recent development, and few examples have been reported for coinage metals. In terms of bimetallic clusters composed of palladium and coinage metals, silver remains the outlier, with copper and gold both represented in literature.[20,21] Tsukuda and coworkers reported gold-rich frameworks of the type $HPd@Au_{10}$ and trimetallic systems $HPd@M_2Au_8$ (M = Ag, Cu).[22] With respect to silver-doped frameworks, Lee and coworkers reported the superatomic rhodium NC $[RhH@Ag_{24}(SPhMe_2)_{18}]^{2-}$, which contains a RhH unit.[23] Recently our group reported PtH-containing 8-electron superatoms of the type $[PtHAg_{19}\{E_2P(O^nPr)_2\}_{12}]$(E = S, Se).[18] After our seminal work on the inclusion of Pd into an Ag_{12} icosahedron in 8-electron clusters of the types $[PdAg_{20}(dtp)_{12}]$ (dtp = dithiophosphate),[24] and $[PdAg_{20}(dsep)_{12}]$ (dsep = diselenophosphate),[25] we now turn our attention to PdH-doped silver superatoms. Three new NCs are reported, $[PdHAg_{19}(dtp)_{12}]$ **1**, $[PdHAg_{20}(dtp)_{12}]$(TFA) ([**2**](TFA)); TFA = trifluoroacetate) and $[PdAg_{21}(dtp)_{12}](BF_4)$ ([**3**](BF_4)). The composition and structural properties are determined by single-crystal X-ray diffraction, X-ray photoelectron spectroscopy (XPS), ESI-TOF-MS, UV-vis, and multinuclear NMR spectroscopy. The screening of effective reagents for the facile conversion of the Ag shell are explored and monitored by in-situ NMR studies. The effect of the solvation sphere on the dynamics of the isomerization in solution is also investigated by VT-NMR. The screening of silver precursors and organic acids for silver framework modifications indicates the intricate role counter ions can play in NC modification, beyond the role of spectators.

Results and Discussion

Synthesis and Reactivity

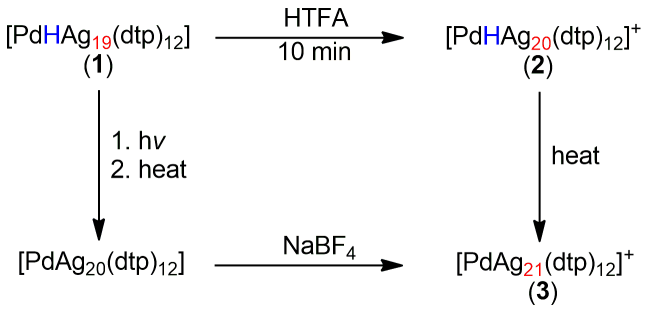

Scheme 1. Synthetic protocol for the controlled modification **1** to yield **2** and **3** while retaining superatomic character.

The parent cluster **1** is isolated from the co-reduction of $[Ag(CH_3CN)_4](BF_4)$ and $[Pd(OAc)_2]$ by $NaBH_4$ in the presence of $[NH_4][S_2P(O^iPr)_2]$ in a 19:1:12 molar ratio (Scheme 1). After purification by column chromatography, **1** is isolated in ~17 % yield. The one-pot reaction yields a mixture of products along with the target compound and the non-hydride Pd-centered NC $[PdAg_{20}\{S_2P(O^iPr)_2\}_{12}]$.[25] Notably, in the preparation of **1,** we found no evidence for the presence of **2** in the same pot. To confirm the presence of the hydride in the clusters, $NaBH_4$ was substituted by $NaBD_4$ with the same synthetic protocol to obtain the deuteride analogues $[Pd(D)Ag_{19}(dtp)_{12}]$ $\mathbf{1_D}$ and $[Pd(D)Ag_{20}(dtp)_{12}]$TFA $\mathbf{2_D}$. Adding a single Ag atom to the shell occurs under acidic conditions, but is only induced by the addition of selected anions. The addition of HTFA or HBF_4 results in the formation of **2**, with the largest selectivity/yield achieved with TFA. Importantly the addition of any acid does not necessarily accommodate this transition. Notably, HOAc leaves **1** intact. In contrast to the addition of the acetic acid, the addition of silver acetate results in a modification of the passivating outer shell after hydride loss, yielding $[PdAg_{20}\{S_2P(O^iPr)_2\}_{12}]$. Furthermore, adding silver salts, [Ag(TFA)] and $[Ag(BF_4)]$, to **1** also yields **2** but with poorer selectivity, resulting in the formation of several by-products and no improvement in the isolated yield. We propose that the transfer occurs *via* an inter-cluster reaction between two molecules of **1,** with the donor cluster scavenged during the formation of **2**. The transfer occurs in solution due to the lability of the ligand shell at room temperature, evident from the VT NMR behavior (Figure S2). The identical ligand framework supports the harvesting of a capping atom from the donor cluster. Thus, the steric and electronic transition is more efficient than adding a virgin silver atom from a precursor salt. A similar screening process was undertaken for the controlled transformation of $[PdAg_{20}(dtp)_{12}]$ to **3**. $NaBF_4$ was found to be the optimal reagent for the modification of $[PdAg_{20}(dtp)_{12}]$ to **3**. This provides further evidence for the ability of counter-anions to play a role in the customization of NCs.[26] In all cases, the transitions prefer the retention of the 8-electron superatomic core.

The second type of inter-cluster reaction results in the conversion of the shell without the need for an additional reducing agent but with loss of the central hydride, indicating self-reduction.[27] In comparison to the homometallic $[Ag_{20}(dtp)_{12}]$ ($Ag@Ag_{19}$), which is prepared from the addition of $NaBH_4$ to $[Ag_{21}(dtp)_{12}]^+$ ($Ag@Ag_{20}$),[13] $[PdHAg_{19}(dtp)_{12}]$ **1** and $[PdHAg_{20}(dtp)_{12}]^+$ **2** undergo an internal redox process in solution to form $[PdAg_{20}(dtp)_{12}]$ and $[PdAg_{21}(dtp)_{12}]$ **3,** respectively.[28] The process can be accelerated by heat and monitored by ^{31}P-NMR, the conversion of **1** to $[PdAg_{20}(dtp)_{12}]$ is given in Figure S14, and shows the transition occurring over a period of 48 hours at 60 °C. The time-dependent ^{1}H NMR indicates the formation of hydrogen gas and a corresponding loss of the hydride resonance, Figure S15. A similar trend is observed for the conversion of **2** to **3** in the ^{31}P NMR, Figure S16. However the evolution of hydrogen gas is not observed, due to anion present in **2**. The transition at ambient conditions takes 2 weeks, and can be monitored by UV/vis spectroscopy (Figure S17). The two-week transition further indicates the stability of the hydride-doped core, at ambient conditions.

The compositions of clusters **1**-**3** were confirmed by ESI-TOF-MS spectrometry, and a comparison of experimental and simulated spectra is presented in Figure 1. The experimental and simulated isotopic patterns show agreement. The mass spectrum of **1** shows a prominent *m/z* peak at 4823.4185 *m/z* assigned to the silver adduct $[\mathbf{1} + Ag]^+$ (calc. 4823.2163). Due to the ambiguous nature of a silver adduct in the current system, cesium iodide was added to the sample prior to analysis to obtain a cesium adduct $[\mathbf{1}+Cs]^+$ observed 4847.4653 m/z (calc. *m/z* 4847.2204) (Figure 1a). The spectrum of **2** contains a molecular ion peak $[\mathbf{2}]^+$ at *m/z* 4823.4185 (calc. *m/z* 4823.2163) (Figure 1b). The deuterated analogues, $\mathbf{1_D}$ and $\mathbf{2_D}$, also showed similar fragmentation patterns with peaks $[\mathbf{1_D}+Ag]^+$ at 4824.2202 *m/z* (calc. *m/z* 4824.2227) and $[\mathbf{2_D}]^+$ at *m/z* 4824.5447 (calc. *m/z* 4824.2227), Figure S1. Similarly, the fragmentation peak observed in **3** corresponds to $[\mathbf{3}]^+$ with *m/z* 4930.5205 (calc. *m/z* 4931.1133) (Figure 1c). The composition of the clusters was further confirmed by X-ray photoelectron spectroscopy (XPS); the percentage compositions and spectra are shown in Figure S13. The spectra explicitly indicate the presence of both Pd and Ag in ratios similar to the expected molecular composition. Furthermore, the spectra indicate the oxidation state of Pd to be zero and the Ag approaching Ag(I) for **1-3**, Figure S13.[29]

The hydride provides a unique probe for configuration changes in the metallic framework due to the coupling with its surrounding silver atoms. The integration ratios of the ^{1}H NMR spectra for **1** and **2** indicate 12 dtp ligands to one hydride. At ambient temperature (293 K) in CD_2Cl_2, the encapsulated hydride moves inside its Ag_{12} icosahedral prison, with a multiplet resonance observed at -8.56 ppm (**1**) and -8.39 ppm (**2**) (Figure S7a and S7c). The broad shape of the peak indicates that the hydride indiscriminately couples to all 12 atoms.

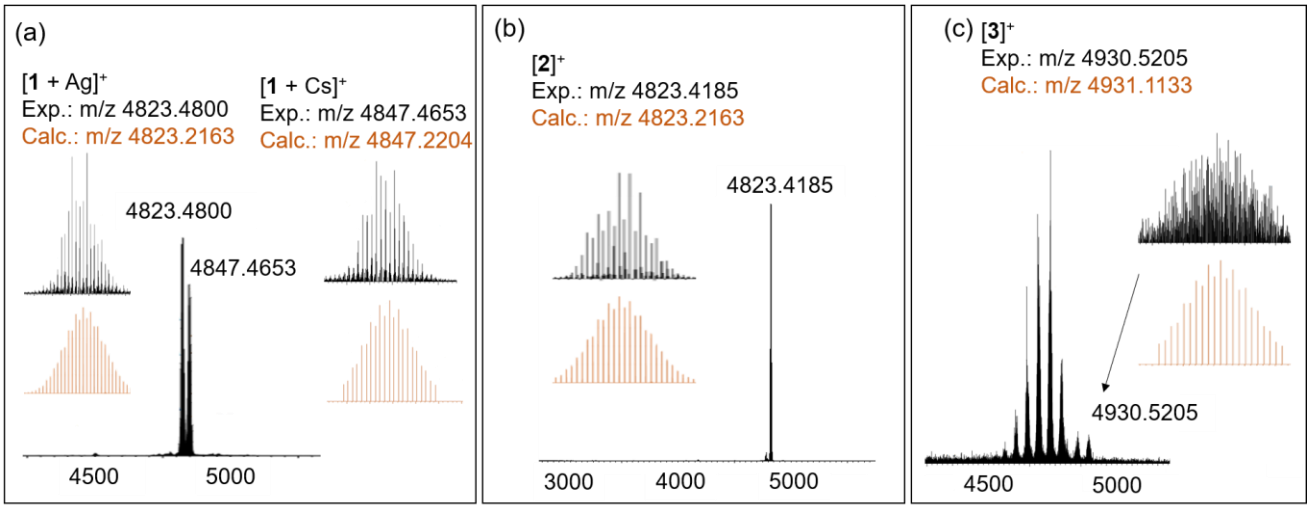

Figure 1. Experimental (black) and simulated (brown) ESI-TOF-MS spectrums for **1(a)**, **2(b)**, and **3(c)**.

The corresponding deuterated resonance in the ^{2}H NMR spectra of $\mathbf{1_D}$ and $\mathbf{2_D}$ confirms the position and magnetic state of the hydride with relatively similar resonances observed at δ = -8.41 ppm and δ = -8.33 ppm for $\mathbf{1_D}$ and $\mathbf{2_D}$, respectively (Figure S7b and S7d). The dynamics of the nanoclusters in solution have been investigated with multinuclear VT-NMR (Figures S2-S5). Reduction in temperature to 173 K decreases the hydride mobility, resulting in a well-defined quartet observed at -8.97 ppm ($^{1}J_{1H\text{-}107Ag}$ = 55.6 Hz, $^{1}J_{1H\text{-}109Ag}$ = 63.9 Hz) and -8.38 ppm ($^{1}J_{1H\text{-}107Ag}$ = 52.7 Hz, $^{1}J_{1H\text{-}109Ag}$ = 60.6 Hz) for **1** and **2,** respectively (Figure 2). The quartet resonance corresponds to the hydride position found in the solid state, wherein the hydride couples with three equivalent Ag atoms while occupying a tetrahedral position (Figure 3a). A similar observation to the related Pt centered NC was previously reported.[18] ^{1}H NMR splitting patterns obtained from simulation are in good agreement with the experimental results and are shown in Figure S6. A comparison of the hydride behavior in **1** and **2** indicates similar environments, with the hydride seemingly unperturbed by the external cluster rearrangements in CD_2Cl_2. The hydride behavior is also in stark contrast to those observed in $[RhH@Ag_{24}(SPhMe_2)_{18}]^{2-}$ wherein the hydride position, inferred from NMR and DFT calculations, indicate preferential bonding to the central Rh atom, with minimal interaction with the Ag framework.[23]

The external configuration of the cluster can be monitored by ^{31}P NMR. At ambient conditions in CD_2Cl_2, a single peak is observed at 101.38, 98.72, and 97.43 ppm for **1**, **2** and **3**, respectively. The reduction in temperature and the concurrent decrease in lability of the ligand shell results in the singlet peak in **1** spreading over a range of 105 – 96 ppm, giving rise to 12 well-resolved peaks at 173 K in CD_2Cl_2 (Figure 2a). Each peak corresponds to a unique phosphorus environment (non-symmetric) for each of the twelve dtp ligands, corresponding to the C_1 symmetry of **1** (vide Infra.). In **2,** a similar trend is observed in CD_2Cl_2. However, four dominant peaks are observed, attributed to the C_3 isomer found in the solid state (Figure 2b). The various changes in symmetry caused by the movement of the outermost shell are more apparent in $(CD_3)_2CO$. At ambient conditions, the hydride resonance follows suit with the CD_2Cl_2 experiments, with peaks at -8.66 ppm (**1**) and -8.59 ppm (**2**). However, in $(CD_3)_2CO$, a decrease in temperature results in the formation of two distinct broad peaks at 173K without the resolution of the quartet recorded in CD_2Cl_2.

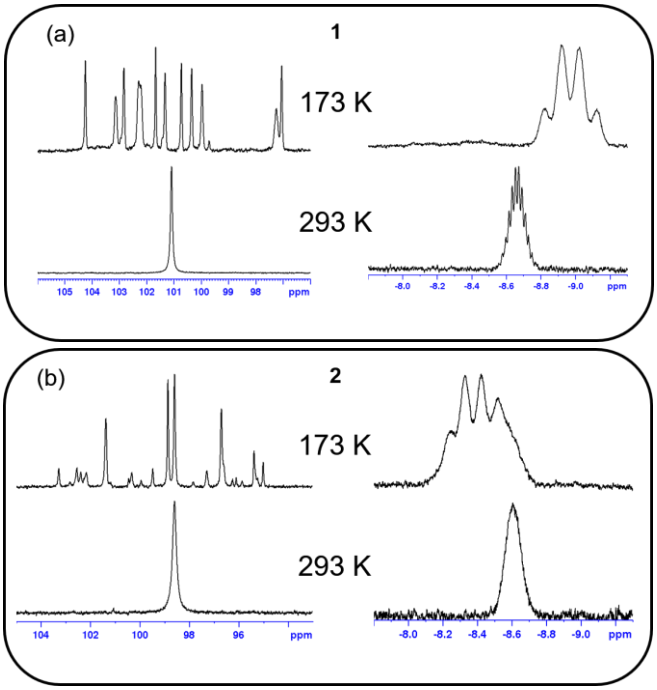

Figure 2. $^{31}P\{^{1}H\}$ NMR (CD_2Cl_2) (left) indicating the lability of the ligand environment at 293 K, and the isomeric distribution observed at 173 K for **1 (a)** and **2 (b)**. ^{1}H NMR (CD_2Cl_2, δ) (right) illustrating the formation of a quartet resonance peak at 173 K for both **1 (a)** and **2 (b)**.

In $(CD_3)_2CO$, there are magnetically distinct environments for the hydride in both **1** and **2**, with a pair of resonances observed (Figure S4b-5b). The ^{31}P NMR is more complex in $(CD_3)_2CO$, with several peaks observed for **1** and **2** suggesting the presence of several isomers resulting from the lability of the peripheral silver layer, Figure S4a-5a. This lability is directly related to the interaction with the solvation sphere and is evident by the differential isomeric distributions in CD_2Cl_2 and $(CD_3)_2CO$. The presence of the counter anion TFA^- in **2** was confirmed by ^{19}F NMR, with singlet resonance observed at -76 ppm, Figure S8. Similarly, the BF_4^- anion in **3** is observed as a singlet at -154.9 ppm and -155 ppm, for isotopes ^{10}B and ^{11}B respectively, Figure S11.

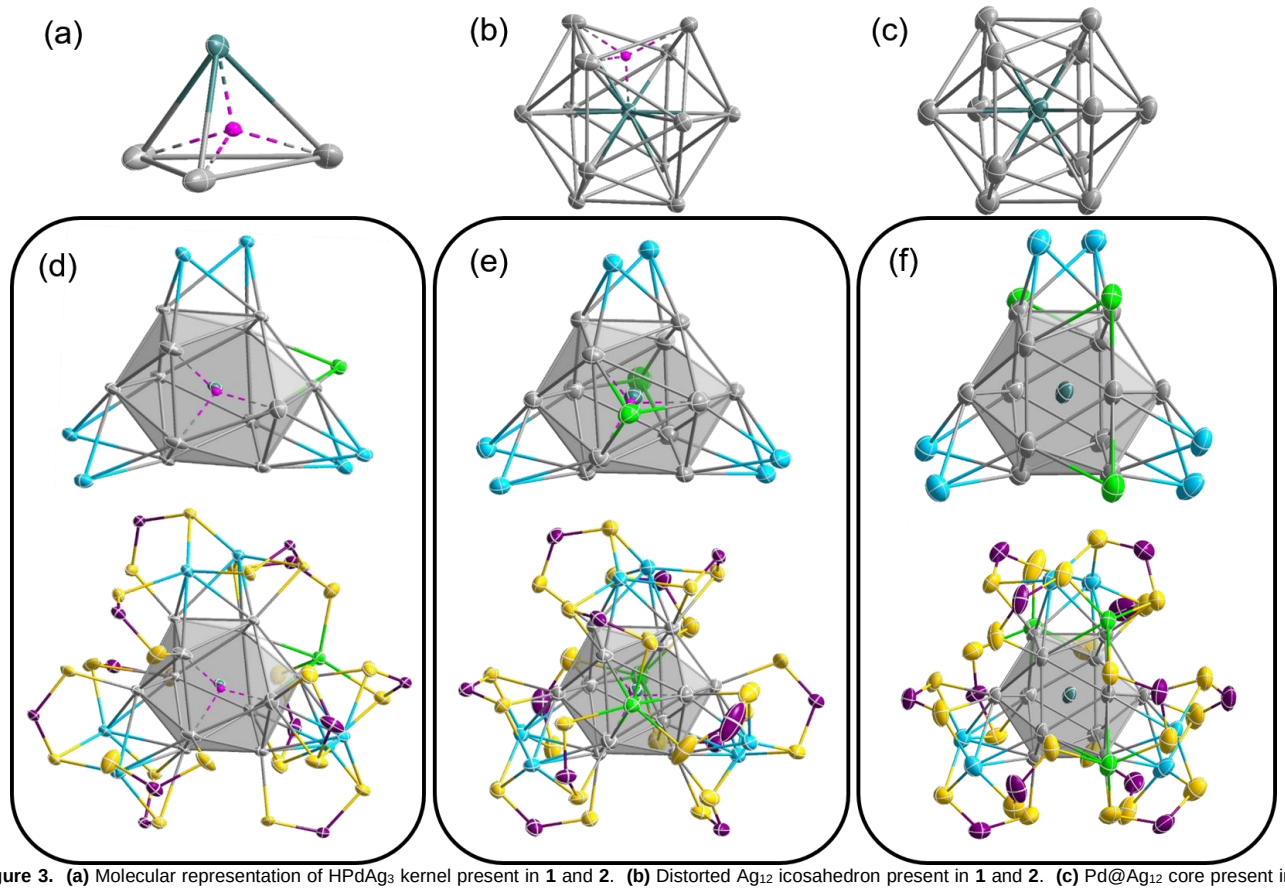

Figure 3. **(a)** Molecular representation of $HPdAg_3$ kernel present in **1** and **2**. **(b)** Distorted Ag_{12} icosahedron present in **1** and **2**. **(c)** $Pd@Ag_{12}$ core present in **3**. The thermal ellipsoid plot of 1-**3** **(d-f)** illustrates the symmetry induced by the capping atoms, with the primary Ag cap occupying symmetrically favorable positions on the triangular facets of the icosahedron. The remaining capping atoms, Ag cap' and ligand stabilization result in the following symmetry for the metallic framework C_1 for **1 (d)**, C_3 for **2 (e)** and C_1 for **3 (f).** (Color code. Pd: dark green; H: pink; Ag: grey; Ag_{cap}: blue; Ag_{cap}': light green; S: yellow; P: purple)

Single-crystal X-ray diffraction data collected for **1**, **2** and **3** were of ample quality that electron density consistent with the hydride dopant in **1** and **2** could be assigned from the difference density map and their positions were subsequently confirmed by density functional theory (DFT) calculations (*vide infra*). Molecular representations are illustrated in Figure 3, with selected bond lengths and angles given in Table 1.[30] Refinements and crystallographic data are provided in Table S1. All structures contain a 12-atom silver icosahedron centered by a PdH unit in **1** and **2** and a Pd atom in **3** (Figure 3d-f). The encapsulated Pd-H motif causes a significant distortion of the Ag_{12} icosahedron, highlighted by the continuous symmetry measure (CSM) values of 0.22 and 0.14 for **1** and **2,** respectively (Figure 3b). In contrast, the Pd-centered Ag icosahedron of **3** approaches an idealized geometry with a CSM value of 0.04 (Figure 3c). The icosahedron distortion in **1** and **2** is also evident in examining the bond distances, as illustrated by a plot of the bond distance as a function of occurrence (Figure S12). Furthermore, the bond distances in **1** and **2** (Table 1) are significantly longer in average than in **3**, in order to accommodate the hydride. Importantly, the core is geometrically similar to the Pt derivative previously reported, in which *neutron diffraction confirmed the position of the hydride*.[18] The tetrahedron encapsulation of the hydride is substantially different from that in the Tsukuda's $HPd@Au_{10}$ frameworks, which contain incomplete icosahedra providing a missing vertex for the hydride to occupy.[21,22] Furthermore, the similarity in the core dimensions of **1**-**3**, indicate the hydride occupies an interstitial tetrahedral site. Due to hydrogen atom being sufficiently small, the overall metal framework is retained. The stability of the interstitial alloy is demonstrated in solution at ambient conditions and in the catalytic application in aqueous medium, described in this report. In the solid state, the outer layer of silver atoms in **1**-**3** can be divided into two groups, Ag_{cap} (blue) and Ag_{cap}' (green), as depicted in Figure 3d-f. Six Ag_{cap} atoms occupy similar triangular faces of the Ag_{12} icosahedron in all clusters. They are grouped by pairs, occupying adjacent faces of the icosahedron, in such a 3-fold fashion that the resulting $(A)@Ag_{12}@(Ag_{cap})_6$ (A = PdH,**1** and **2**; A = Pd, **3**) framework have an ideal C_{3v} symmetry. (Figure 3d-f). Adding now the unique green Ag_{cap}' in **1** results in a complete loss of symmetry (Figure 3d). The same situation occurs when adding the two Ag_{cap}' in **3** (Figure 3f). In contrast, the two Ag_{cap}' in **2** occupy positions along the Pd-H motif, resulting in the preservation of C_3 axis, (Figure 3e). The M_{22} (M_1Ag_{21}) configuration in **3** is the first report of such stabilized by dichalcogenolato ligands and is exceedingly rare in literature.

Table 1. Selected metal bond lengths and geometry parameters.

	1	**2**	**3**
CSM	0.22	0.14	0.04
Pd_{cen}-Ag_{ico}	2.7129(7)-2.9793(12)	2.756(2)-2.829(2)	2.721(2)-2.778(2) Å,
(Å)	avg. 2.7926	avg. 2.793(2)	avg. 2.752(2)
Ag_{ico}-Ag_{ico}	2.8124(8)-3.2135(11)	2.808(2)-3.227(2)	2.854(2)-2.995(2) Å,
(Å)	avg. 2.9204(8)	avg. 2.936(2)	avg. 2.702(2)
Ag_{ico}-Ag_{cap}	2.8911(8)-3.1254(7)	2.921(2)-3.231(2)	2.660(2)-3.120(4)
(Å)	avg. 2.9915(8)	avg. 3.003(2)	avg.2.702 (3)
Ag_{ico}-Ag_{cap}'	2.8952(8)-3.0191(8)	2.975(2)-3.012(2),	2.857(3)-3.085(3) Å,
(Å)	avg. 2.9624(8)	avg. 2.990(2)	avg. 2.945(2)

Only few examples of bimetallic system are present, in particular those with M_{13} centered-icosahedral kernels: monometallic Ag_{22} protected by nitrogen donor ligands [31] and M_1Ag_{21} (M = Au/Ag) stabilized by 1,1'-bis-(diphenylphosphino)ferrocene ligands.[32] To our knowledge no reports on group 10 doped M_{22} frameworks can be found in literature. The stabilizing ligand shell accommodates the silver framework in such a way each capping Ag is approximately planar-tricoordinated. The twelve dtp ligands in cluster **1** of C_1 symmetry can be classified by connectivity with one η^2 (μ_1, μ_1), three η^4 (μ_2, μ_2) and eight η^3 (μ_2, μ_1). In cluster **2** of C_3 symmetry, two coordination environments can be found, with three η^3 (μ_2, μ_2) and nine η^3 (μ_2, μ_1). In cluster **3** of C_1 symmetry, one ligand is η^2 (μ_1, μ_1), three are η^3 (μ_2, μ_1) and eight are η^4 (μ_2, μ_2).

Whereas the NMR analysis indicates the presence of isomers in solution, only one isomer is found for each cluster in the solid state. It is possible to elaborate a geometrical prediction of the most probable isomers, by analogy with the known dicalcogenolate-protected 8-electron clusters having Ag_{20} and MAg_{20} kernels. Furthermore, these predictions are supported by DFT calculations discussed below. As mentioned above, both frameworks of **1** and **2** contain the same $(PdH)@Ag_{12}@(Ag_{cap})_6$ sub-unit of ideal C_{3v} symmetry ($PdHAg_{18}$ in Figure 4). Assuming that this very recurrent motif[12,14,33] is preserved in all the clusters discussed here, the nature of the possible isomers depends on the distribution of the supplementary Ag_{cap}' (green) atoms on the available triangular faces of the Ag_{12} icosahedron. Adding one Ag_{cap}' atom to the $PdHAg_{18}$ C_{3v} framework in Figure 4 allows to generate four different topologies. When added on the C_3 axis, the C_{3a} isomer of **1** is generated, the metal arrangement of which being that of $[Ag_{20}\{S_2P(dtp\}_{12}]$.[13] Three additional structures, all of C_1 symmetry, can be generated by capping each one of the three symmetry-independent faces of $PdH@Ag_{18}$ that do not intersect the C_3 axis. One of them is the solid-state structure of **1**, also reported for the Pt derivative.[18] We propose discarding the two other C_1 structures, since no report of these topologies exist so far in this chemistry. On the other hand, we suggest another C_3 structure (C_{3b}), derived from the *T* structure of $[PdAg_{20}(dsep)_{12}]^+$ [34] by the removal of one capping Ag. Alternatively, C_{3b} can be derived from C_{3a} by a concerted rotational displacement of three Ag_{cap} atoms, making them of the Ag_{cap}' type, as illustrated in Figure 4. Adding now two Ag_{cap}' atoms along the C_3 axis of the $PdH@Ag_{19}$ framework generates the X-ray C_3 structure of **2**. Actually, there are several additional possibilities to distribute the two Ag_{cap}' on the available positions of $PdHAg_{18}$ in such a way that at least one Ag_{cap}' is not on the C_3 axis. We propose to retain three structures of C_1 symmetry in which none of the Ag_{cap}' atom is on the C_3 axis, but which have been reported for $[MAg_{20}\{S_2P(O^nPr)_2\}_{12}$ (M = Pd, Pt),[24,17] $[PdAg_{20}\{E_2P(O^iPr)_2\}_{12}$ (E = S, Se),[25] and $[AuAg_{20}\{S_2P(O^iPr)_2\}_{12}]$,[16] respectively ($C_{1a}$, C_{1b} and C_{1c} in Figure 4). Owing to the complexity of the ligand topology in **3** and the uniqueness of this $M@Ag_{21}$ structure, no reasonable isomer of **3** could be proposed. The relative energies of the isomers of clusters **1** and **2** depicted in Figure 4 were computed through DFT calculations at the BP86/Def2-TZVP level of calculations (see Computational Details in the SI). For the sake of computational limits, the dtp ligands were replaced by S_2PH_2, a simplification which has been proved to be reasonable in many past investigations.[7, 12-18, 20,24, 25, 27, 33] The optimized geometries of the three structures found in the solid state match with their experimental counterpart, in particular with respect to the hydride location in **1** and **2**. Selected computed data are provided in Table 2. The experimental structures of **1** and **2** correspond to the most stable computed isomers, both in total (ΔE) and free (ΔG) energies. However, the energy differences between isomers remain small, as usually found in this family of compounds.[13,33] Owing to the considered level of theory and modelling, the computed relative energies are consistent with the existence of several isomers in solution. Those considered in our calculations constitute good candidates, although other 8-electron isomers, also differing from the spatial configuration of their outer shell, (including in the case of **3**) are possible. In fact, all the computed data of the **1**-**3** systems reported in Table 2 are very similar. Their atomic charges computed from natural atomic orbital (NAO) analysis and their Wiberg bond indices (WBIs) are consistent with the view of the outer capping atoms being in the formal +I oxidation state and only weakly bonded to the Ag_{ico} triangle they are capping.[12,15,33] Neglecting this capping interaction, they can be viewed as stable 16-electron trigonal planar AgS_3 metal centers, leaving the centered icosahedral kernel with an 8-electron *superatomic* count. Since the computed isomers of **1** and **2** display very similar features, we comment below only the most stable structures, *i.e.* that characterized in the solid state. Their Kohn-Sham orbital diagrams (Figure S23), illustrate their $1S^2\ 1P^6\ 1D^0$ *superatomic* configuration, with the 1P and 1D levels (plotted in Figure S24) being the frontier orbitals. The electronic structure of **1** is very similar to that of its $[PtHAg_{19}(dtp)_{12}]$ relative.[18] The H-Pd and H-Ag WBI values (Table 2) indicate that the hydrogen atom interacts preferentially with Pd, although the H-Ag interaction is not as weak as in $[PtHAg_{19}(dtp)_{12}]$.[18] The Pd-H interaction, which is sketched for an isolated Pd-H unit in Figure 5, involves primarily a $4d_z^2$(Pd) orbital. Owing to the strong destabilization of the σ^*(Pd-H) orbital, the unpaired electron prefers occupying the orbital of large 5s(Pd) character, *i.e.* that which mainly contributes to the building of the *superatomic* orbitals. Thus, the contribution of PdH to the *superatomic* electron count is 1, similarly to Ag ($4d^{10}\ 5s^1$). $[(PdH)@Ag_{19}(dtp)_{12}]$ (**1**) and $[(Ag)@Ag_{19}(dtp)_{12}]$[13] are strongly related 8-electron superatoms, the former being however somewhat axially distorted. Thus, though the hydride participation to the superatomic orbitals is low, its electron should be included in the superatomic count. The electronic structure of **2** is essentially the same as that of **1**, with a similar 8-electron $[(PdH)@Ag_{12}]^{5+}$ icosahedral core. That of **3** is strongly related to those of $[PdAg_{20}\{S_2P(O^nPr)_2\}_{12}]$[24] and $[PdAg_{20}\{S_2P(O^iPr)_2\}_{12}]$,[25] which have one less Ag(I) capping atom.

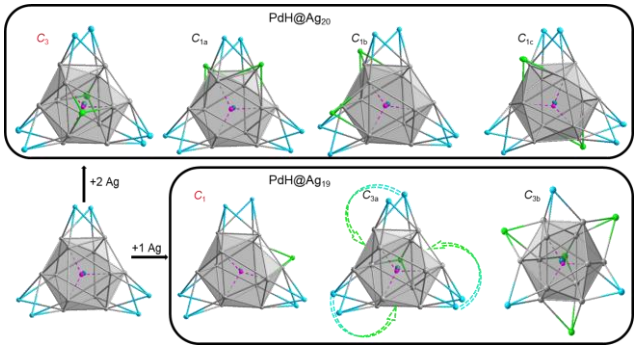

Figure 4. Inferred isomeric distribution in **1**, and **2** with crystallographic confirmed isomers with red labels. (Color code. Pd: dark green; H: pink; Ag: grey; Ag_{cap}: blue; $Ag_{cap'}$: light green)

Table 2. Selected DFT-computed data for **1**, **2** and **3**. Distances are in Å and their corresponding Wiberg bond indices into brackets.

Isomer		**1** C_1	**1** C_{3a}	**1** C_{3b}	**2** C_3	**2** C_{1a}	**2** C_{1b}	**2** C_{1c}	**3** C_1
ΔE (kcal/mol)		0.0	1.9	0.9	0.0	6.6	6.2	4.6	
ΔG (kcal/mol)		0.0	1.7	1.8	0.0	4.1	3.1	1.7	
$\Delta E_{HOMO-LUMO}$ (eV)		1.67	1.85	1.96	1.86	1.56	1.66	1.51	1.37
NAO charges (avg.)	H	-0.46	-0.43	-0.46	-0.46	-0.44	-0.44	-0.44	
	Pd	-1.01	-0.99	-0.96	-1.04	-1.00	-0.98	-1.00	-1.18
	Ag_{ico}	+0.36	+0.35	+0.35	+0.35	+0.34	+0.34	+0.34	+0.27
	$Ag_{cap}/Ag_{cap'}$	+0.70	+0.70	+0.71	+0.71	+0.70	+0.71	+0.71	+0.70
Pd_{cen}-H		1.718 [0.138]	1.713 [0.143]	1.690 [0.141]	1.722 [0.113]	1.715 [0.142]	1.703 [0.148]	1.709 [0.145]	
Ag_{ico}-H (avg.)		2.004 [0.115]	1.984 [0.112]	1.967 [0.113]	1.979 [0.129]	2.001 [0.115]	2.010 [0.109]	2.039 [0.110]	
Pd_{cen}-Ag_{ico} (avg.)		2.888 [0.141]	2.885 [0.143]	2.894 [0.143]	2.884 [0.146]	2.887 [0.138]	2.886 [0.136]	2.887 [0.140]	2.847 [0.158]
Ag_{ico}-Ag_{ico} (avg.)		3.019 [0.079]	3.005 [0.082]	3.010 [0.080]	2.997 [0.082]	2.998 [0.082]	3.005 [0.081]	3.003 [0.081]	2.994 [0.085]
Ag_{ico}-$Ag_{cap}/Ag_{cap'}$ (avg.)		3.103 [0.046]	3.093 [0.037]	3.103 [0.033]	3.107 [0.038]	3.123 [0.041]	3.122 [0.041]	3.119 [0.041]	3.102 [0.044]
CSM		0.179	0.089	0.271	0.132	0.189	0.176	0.284	0.048

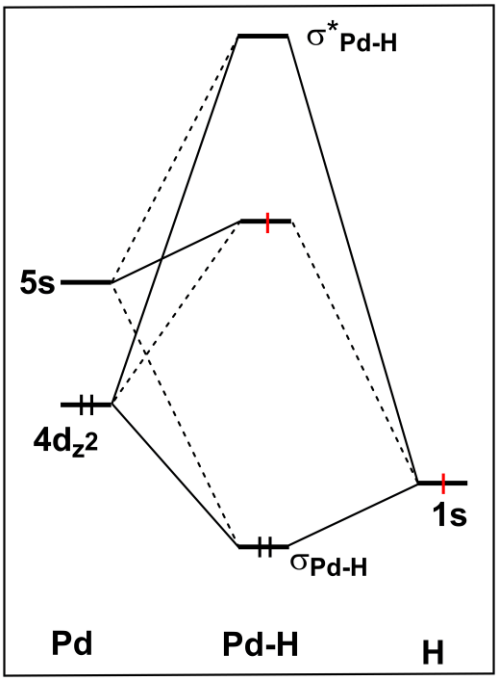

Figure 5. Simplified MO diagram for an isolated PdH unit. The singly occupied orbital of very large 5s(Pd) character is the one which is, together with the 5s(Ag) AOs, principally involved in the building of the *superatomic* orbitals of the $[PdH@Ag_{12}]^{5+}$ cores of **1** and **2**.

The optical properties of the NCs were investigated by UV-vis and PL spectroscopy. The UV-vis spectra of **1** and **2** are relatively similar, with a common peak observed at 405 nm and with marginally different shoulder peaks at 455 and 462 nm for **1** and **2,** respectively (Figure 6). Furthermore, the emission in **3** is red-shifted in comparison to $[PdAg_{20}\{S_2P(O^iPr)_2\}_{12}]$, with a broad emission profile centered at 842 nm in comparison to 741 nm in the latter (Figure S18). The emission lifetime recorded for **3** is 200 μs (Figure S19), which is relatively close to the 235 μs recorded for $[PdAg_{20}\{S_2P(O^iPr)_2\}_{12}]$. The additional silver capping atom has a dramatic influence on the emission profile. Compared to the monometallic 8-electron superatomic species, the luminescent profile in these systems seems more sensitive to shell configuration than the central metal species,[12,13] demonstrating the tunability afforded by atomically precise single-atom tailoring. The TD-DFT UV-Vis spectra simulated at the CAM-B3LYP/Def2-TZVP level (see Computational Details in the SI) of clusters **1**-**3** considered in their respective C_1, C_3 and C_1 solid state configurations are shown in Figure 6b. There is a good agreement with the experimental spectra (Figure 6a), It is noteworthy that the simulated spectra of **1, 2** and $[PtHAg_{19}(dtp)_{12}]$[18] exhibit similar double band shape in the 300-500 nm region. These peaks are of 1P→1D nature, as well as the unique band shown by **3** in the same range.

The reduction of 4-nitrophenol (4-NP) to 4-aminophenol (4-AP) has been chosen as a model reaction to determine the catalytic activity of **1**-**3**. The reaction has been established as a reliable model for the quantitative assessment of nanoparticle catalytic activity.[35,36] The mechanism has been extensively studied for silver nanoclusters.[37] More recently, it has been applied to NCs, due to the ability to analyze the reaction by routine UV-vis spectrometry quantitatively.[38,39] The hydrolysis of $NaBH_4$ in aqueous media results in the deprotonation of 4-NP to yield 4-nitrophenolate ($4NP^-$).

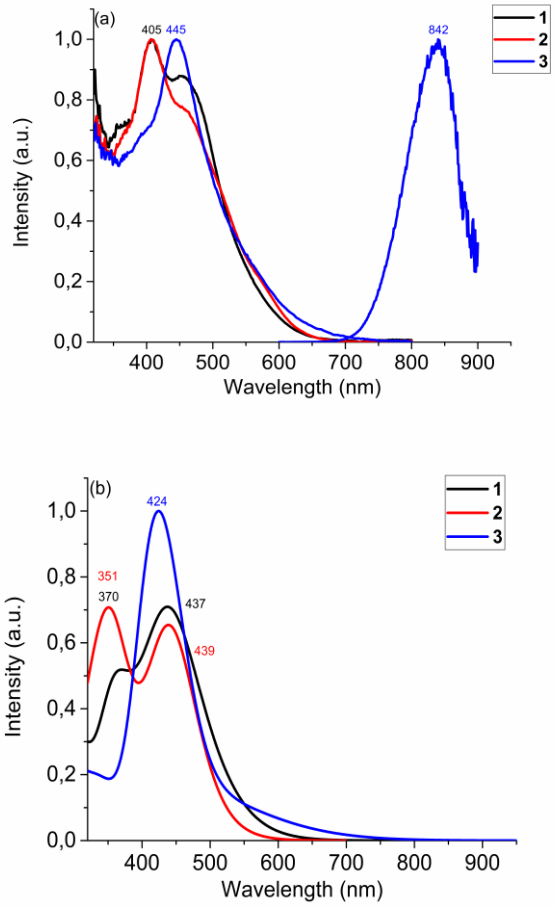

Figure 6. a) UV-vis absorption spectra for **1**-**3**, and emission spectrum of **3** (λex = 448 nm) recorded in CH_2Cl_2**. b)** TD-DFT-simulated UV-vis spectra for **1**-**3** in their respective C_1, C_3 and C_1 solid state configurations.

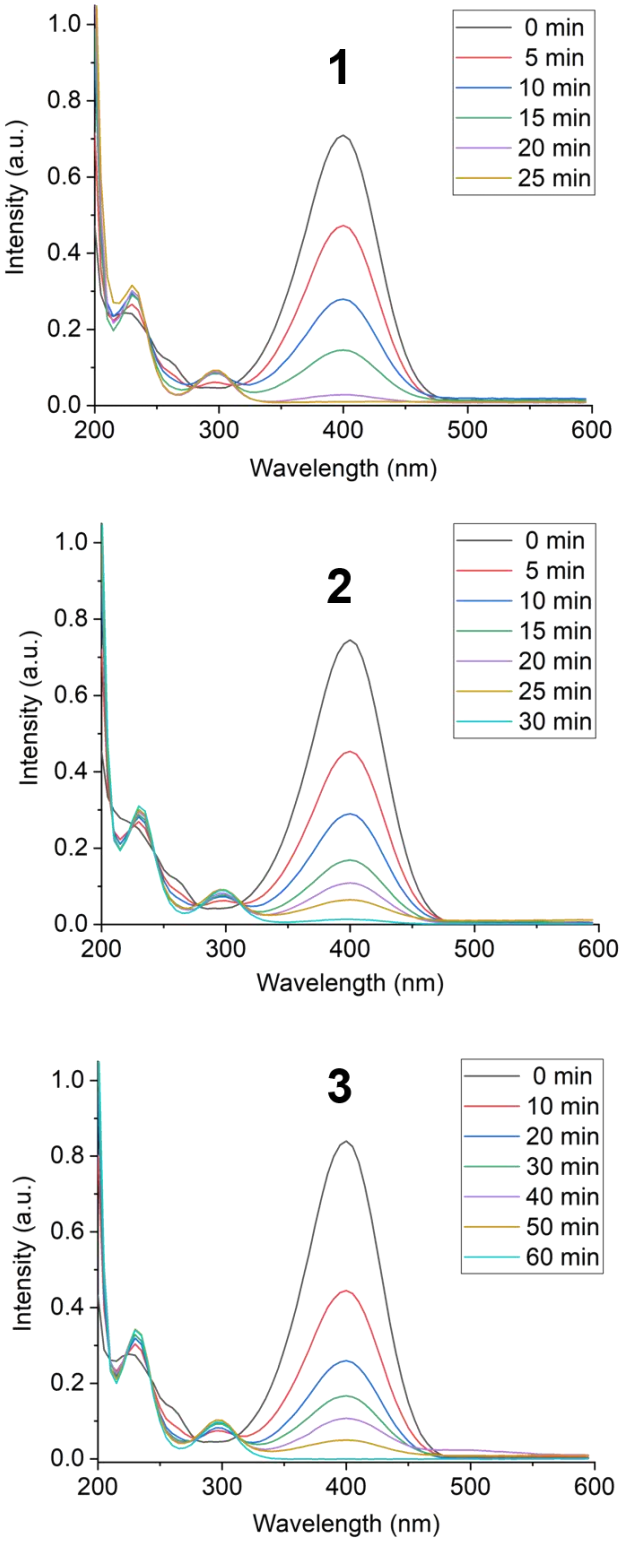

Figure 7. Uv-vis spectra showing reduction of 4-nitrophenol catalyzed by **1**, **2** and **3**, in the presence of $NaBH_4$.

The $4NP^-$ has a strong absorption band at 400 nm allowing for facile quantitative analysis of the 4NP reduction. In the current context, the precision afforded by ligand-protected NC's enables the development of uniform catalysts tailored atom by atom. It is therefore, appropriate to determine the comparative influence of kernel and shell modifications on the catalytic efficacy. The UV-vis absorption spectra for the catalytic reduction of 4-NP, with **1-3,** are given in Figure 7. The reduction is done at room temperature, with a catalytic loading of 10 mol % found to be optimum. The addition of $NaBH_4$ is capped at 20 mol eqv. Excessive amounts of $NaBH_4$ decrease the catalytic activity and result in the catalyst's decomposition. The complete conversion of the 4-NP is achieved within 25, 30, and 60 min for **1**-**3**, respectively. All clusters perform the reduction with the hydride-doped clusters **1** and **2**, superior to **3**, solely based on the rate of decay, Figure S21. The calculated apparent rate constant, *k* for **1**, **2**, and 3 are 0.1195 min^{-1}, 0.0901 min^{-1} and 0.0509 min^{-1}, respectively. Fundamentally, the steric factors involved in the approach of the reactants to the catalytic site (Ag atom) in **1**-**3**, appear to be similar, as seen in the space-filling representations in Figure S22. The Ag atoms are accessible in all instances, however with the complexity of the dynamic behavior of the cluster at ambient conditions, it is difficult to confirm the reaction mechanism directly, although the linear correlation of the $\ln(C/C_0)$ vs. time corresponds to the Langmuir-Hinshelwood model for the reduction. We tentatively propose that the reduction follows first-order kinetics. The catalyst has reasonable stability in an aqueous environment and the differential solubility allows for facile separation and reuse. The catalyst remains active for at least 4 catalytic runs with an increase time required for complete conversion. A flaw of bare Ag nanoparticles is the oxidation of the surface silver atoms during the catalytic cycles and the formation of AgO layer over the catalytic surface. In the current report, the dtp ligands, act as protecting layer. Importantly the absence of support implies that the cluster is solely responsible for the catalytic activity, both the electronic and steric factors governing the reduction.

Conclusion

This report demonstrates the ability to control cluster composition at the kernel and shell levels. This allows for the atomic-level manipulation of the electronic and physical properties of the NC. Judicious choice of *'non-innocent'* spectator anions, and the form in which they are introduced, play a crucial role in dictating the nature of the isolated product. The formation of these new NCs and the transitions between them have been confirmed by multinuclear NMR, mass spectroscopy and crystallography. Modifications of the parent cluster $[Pd(H)Ag_{19}\{S_2P(O^iPr)_2\}_{12}]$ **1** result in a practical solubility change with the addition of a single Ag atom to yield $[Pd(H)Ag_{20}\{S_2P(O^iPr)_2\}_{12}]TFA$ **2**. In both **1** and **2**, the interstitial hydrogen provides to the central Pd atom with the electron it misses to complete the *superatomic* 8-electron count with the other metals (in other words, PdH is isoelectronic with Ag). The removal of the interstitial hydrogen from the cluster together with the addition of a supplementary outer (capping) Ag atom form a luminescent species **3**, a new silver-rich M_{22} species. The catalytic activity of **1**-**3** indicates that the hydride-doped catalysts are superior. The reported physical characteristics will prove to be helpful in inevitable future applications.

Acknowledgements

This work was supported by the National Science and Technology Council in Taiwan (111-2123-M-259-002). and the GENCI French National Computer Resource Center (grant A0030807367).

Keywords: Superatom • Palladium hydride • atomically precise nanoclusters • dithiophosphate

References

[1] T. Graham, *Proc. R. Soc. London* **1869**, *17*, 212–220.

[2] S. N. Khanna, P. Jena, *Phys. Rev. Lett.* **1992**, *69*, 1664–1667.

[3] H. Häkkinen, *Chem. Soc. Rev.* **2008**, *37*, 1847.

[4] M. Walter, J. Akola, O. Lopez-Acevedo, P. D. Jadzinsky, G. Calero, C. J. Ackerson, R. L. Whetten, H. Grönbeck, H. Häkkinen, *Proc. Natl. Acad. Sci.* **2008**, *105*, 9157–9162.

[5] P. D. Jadzinsky, G. Calero, C. J. Ackerson, D. A. Bushnell, R. D. Kornberg, *Science* **2007**, *318*, 430.

[6] S. Jin, S. Wang, M. Zhu, *Chem. - An Asian J.* **2019**, *14*, 3222–3231.

[7] F. Gam, C. W. Liu, S. Kahlal, J. Y. Saillard, *Nanoscale* **2020**, *12*, 20308–20316.

[8] J. Yan, H. Su, H. Yang, S. Malola, S. Lin, H. Häkkinen, N. Zheng, *J. Am. Chem. Soc.* **2015**, *137*, 11880–11883.

[9] X. Liu, J. Yuan, C. Yao, J. Chen, L. Li, X. Bao, J. Yang, Z. Wu, *J. Phys. Chem. C.* **2017**, *121*, 13848–13853.

[10] M. Kim, K. L. D. M. Weerawardene, W. Choi, S. M. Han, J. Paik, Y. Kim, M. G. Choi, C. M. Aikens, D. Lee, *Chem. Mater.* **2020**, *32*, 10216–10226.

[11] S. Hossain, S. Miyajima, T. Iwasa, R. Kaneko, T. Sekine, A. Ikeda, T. Kawawaki, T. Taketsugu, Y. Negishi, *J. Chem. Phys.* **2021**, *155*, 024302.

[12] R. S. Dhayal, J.-H. Liao, Y.-C. Liu, M.-H. Chiang, S. Kahlal, J.-Y. Saillard, C. W. Liu, *Angew. Chem. Int. Ed.* **2015**, *127*, 3773–3777.

[13] R. S. Dhayal, Y. R. Lin, J. -H. Liao, Y. J. Chen, Y. C. Liu, M. H. Chiang, S. Kahlal, J. Y. Saillard, C. W. Liu, *Chem. - A Eur. J.* **2016**, *22*, 9943–9947.

[14] S. Sharma, K. K. Chakrahari, J. Y. Saillard, C. W. Liu, *Acc. Chem. Res.* **2018**, *51*, 2475–2483.

[15] Y.-R. Lin, P. V. V. N. Kishore, J.-H. Liao, S. Kahlal, Y.-C. Liu, M.-H. Chiang, J.-Y. Saillard, C. W. Liu, *Nanoscale* **2018**, *10*, 6855–6860.

[16] J. H. Liao, S. Kahlal, Y. C. Liu, M. H. Chiang, J. Y. Saillard, C. W. Liu, *J. Clust. Sci.* **2018**, *29*, 827–835.

[17] T. -H. Chiu, J. -H. Liao, F. Gam, I. Chantrenne, S. Kahlal, J. Y. Saillard, C. W. Liu, *J. Am. Chem. Soc.* **2019**, *141*, 12957–12961.

[18] T. -H. Chiu, J. -H. Liao, F. Gam, Y. Y. Wu, X. Wang, S. Kahlal, J. Y. Saillard, C. W. Liu, *J. Am. Chem. Soc.* **2022**, *144*, 10599–10607.

[19] C. Sun, B. K. Teo, C. Deng, J. Lin, G.-G. Luo, C.-H. Tung, D. Sun, *Coord. Chem. Rev.* **2021**, *427*, 213576.

[20] K. K. Chakrahari, R. P. B. Silalahi, T. –H. Chiu, X. Wang, N. Azrou, S. Kahlal, Y. Liu, M. Chiang, J. Saillard, C. W. Liu, *Angew. Chem. Int. Ed.* **2019**, *58*, 4943–4947.

[21] S. Takano, H. Hirai, S. Muramatsu, T. Tsukuda, *J. Am. Chem. Soc.* **2018**, *140*, 12314–12317.

[22] H. Hirai, S. Takano, T. Tsukuda, *ACS Omega.* **2019**, *4*, 7070–7075.

[23] H. Yi, S. M. Han, S. Song, M. Kim, E. Sim, D. Lee, *Angew. Chem. Int. Ed.* **2021**, *60*, 22293–22300.

[24] S. K. Barik, T.-H. Chiu, Y.-C. Liu, M.-H. Chiang, F. Gam, I. Chantrenne, S. Kahlal, J.-Y. Saillard, C. W. Liu, *Nanoscale* **2019**, *11*, 14581–14586.

[25] S. K. Barik, C.-Y. Chen, T. –H. Chiu, Y.-R. Ni, F. Gam, I. Chantrenne, S. Kahlal, J. Saillard, C. W. Liu, *Commun. Chem.* **2022**, *5*, 151.

[26] X. Wei, K. Chu, J. R. Adsetts, H. Li, X. Kang, Z. Ding, M. Zhu, *J. Am. Chem. Soc.* **2022**, *144*, 20421–20433.

[27] Y. J. Zhong, J. -H. Liao, T. -H. Chiu, S. Kahlal, C. J. Lin, J. Y. Saillard, C. W. Liu, *Angew. Chem. Int. Ed.* **2021**, *60*, 12712–12716.

[28] W. E. van Zyl, C. W. Liu, *Chem. - A Eur. J.* **2022**, *28*, e202104241.

[29] Y.-G. Wu, J.-H. Huang, C. Zhang, X.-K. Guo, W.-N. Wu, X.-Y. Dong, S.-Q. Zang, *Chem. Commun.* **2022**, *58*, 7321–7324.

[30] Deposition numbers 2218682-2218684 contain the supplementary X-ray crystallographic data for **1** ~ **3** reported in this paper. These data are provided free of charge by the joint Cambridge Crystallographic Data Centre.

[31] S.-F. Yuan, Z.-J. Guan, W.-D. Liu, Q.-M. Wang, *Nat. Commun.* **2019**, *10*, 4032.

[32] X. Zou, S. He, X. Kang, S. Chen, H. Yu, S. Jin, D. Astruc, M. Zhu, *Chem. Sci.* **2021**, *12*, 3660–3667.

[33] F. Gam, I. Chantrenne, S. Kahlal, T. H. Chiu, J. H. Liao, C. W. Liu, J. Y. Saillard, *Nanoscale* **2021**, *14*, 196–203.

[34] W.-T. Chang, P.-Y. Lee, J.-H. Liao, K. K. Chakrahari, S. Kahlal, Y.-C. Liu, M.-H. Chiang, J.-Y. Saillard, C. W. Liu, *Angew. Chem. Int. Ed*. **2017**, 56, 10178–10182.

[35] N. Pradhan, A. Pal, T. Pal, *Colloids Surfaces A Physicochem.* Eng. Asp. **2002**, *196*, 247–257.;

[36] P. Zhao, X. Feng, D. Huang, G. Yang, D. Astruc, *Coord. Chem. Rev.* **2015**, *287*, 114–136.

[37] J. Strachan, C. Barnett, A. F. Masters, T. Maschmeyer, *ACS Catal.* **2020**, *10*, 5516–5521.

[38] Z. J. Guan, R. L. He, S. F. Yuan, J. J. Li, F. Hu, C. Y. Liu, Q. M. Wang, *Angew. Chem. Int. Ed.* **2022**, *61*, DOI 10.1002/anie.202116965.

[39] S.-F. Yuan, Z.-J. Guan, Q.-M. Wang, *J. Am. Chem. Soc*. **2022**, *144*, 11405–11412